Supporting Information

Marcott et al. 10.1073/pnas.1104772108

SI Text

1. Mg/Ca Measurements. Only three species in our core have Mg/Ca temperature calibrations (*Melonis barleeanum*, *Cibicidoides lobatulus*, and *Cibicidoides spp.*), and these species only occurred in sufficient numbers for measurements to bracket the four Heinrich events H1, H3, H5a, H6. Moreover, because the species composition varies downcore, no one species was always available for each depth. At 15 depths, however, we replicated multispecies Mg/Ca measurements, of which 13 replicate at 1 σ and the other two replicate at 2 σ (Table S1). Mg/Ca ratios (mmol/mol) were converted to bottom water temperatures (BWTs) using calibrations developed in the North Atlantic Ocean near Iceland for *M. barleeanum* (1) [$\mathrm{Mg/Ca} = 0.658 \times \exp(0.137 \times \mathrm{BWT})$] and *C. lobatulus* (2) ($\mathrm{Mg/Ca} = 1.10 + 0.129 \times \mathrm{BWT}$). Mg/Ca ratios were converted to BWT for *C. spp.* [$\mathrm{Mg/Ca} = 0.90 \times \exp(0.11 \times \mathrm{BWT})$] using a global calibration (3). The automated flow-through system has an average standard deviation of 0.08 mmol/mol for duplicate Mg/Ca samples (4); combined with the temperature calibration error for the individual benthic species (1–3), the range of propagated uncertainty is 1.0–1.5 °C. Our Mg/Ca BWT error (approximately 1.3 °C) is in agreement with previous work where replicate foraminifera analysis, species calibration, and the carbonate ion ($[CO_3^{2-}]$) effect uncertainties are considered (1, 5, 6).

We measured 111 samples from core EW9302-2JPC and 20 samples from core MD95-2010 (Tables S1 and S2). We also made Mg/Ca measurements on two core-top samples, one on *C.* spp., and one on *M. barleeanum*. Based on 17 hydrographic profiles within 50 km of our core, the range of BWT for depths 1,000–1,500 m is 3.29–3.86 (3.43 ± 0.28 at 2 σ) °C. Our core-top measurements are 4.9 ± 2.6 and 6.3 ± 2.6 °C (2 σ), which overlap at 2 σ. Based on the existing age model, however, it is unlikely that the core top is modern; extrapolating our age model from the two youngest age constraints [Vedde Ash (=12.2 ka) at 16 cm, calibrated ^{14}C age (=16.9 ka) at 32 cm] would suggest the core-top sample (1.5 cm) is approximately 7.5 ka.

2. Age Model. The age model for EW9302-2JPC is based on previously published ^{14}C dates, tephra layers at 16 cm (Vedde Ash) and 408-cm depth (ASH II), and tie points at 496 cm (peak of H6) to the age of peak of H6 determined by correlation to Greenland ice cores (7) and at 544-cm depth to the age of the marine isotope stage 5/4 boundary (8) (Table S1). The age model for MD95-2010 is based on previously published ^{14}C dates (9) that were recalibrated using Calib 6.0 (10) (Table S2).

3. Ice-Rafted Debris. Because the resolution (8 cm) of the original published detrital carbonate (DC) record from core EW9302-2JPC (8) is at a lower resolution than our temperature data, we generated new DC data for the Heinrich layers where we have temperature data from Mg/Ca. We duplicated the original counting protocols and then counted DC from several of the original intervals to demonstrate replication (Fig. S1).

4. Oxygen Isotopes. We made six new δ^{18}O measurements on *C. lobatulus*, *Cibicidoides wuellerstorfi* (each with 0.64 per mil correction for fractionation) and *M. barleeanum* (0.4 per mil correction) from core EW9302-2JPC at the Oregon State University (OSU) Stable Isotope Laboratory for the deglacial interval (20–13 ka) to supplement those already published (8). Prior to stable isotope measurements, benthic species were carefully selected so as to not incorporate "dirty" samples into the analysis. Otherwise, all samples followed previous procedures (11). Sediment samples were cleaned and sieved with deionized water and calgon and dried at 40 °C. One to six specimens of *C. lobatulus*, *C. wuellerstorfi*, or *M. barleeanus* were used for each stable isotope measurement. All benthic foraminifera samples were sonicated in deionized water and methanol. Samples were then dried at room temperature (approximately 25 °C) for 24 h and then analyzed at OSU on a Finnigan-MAT 252 stable isotope ratio mass spectrometer equipped with a Kiel-III carbonate device. Samples were reacted at 70 °C in phosphoric acid, and all data are reported relative to the Pee Dee Belemnite standard through our internal standard, which is regularly calibrated against NBS-19.

We calculated the ice-volume corrected benthic δ^{18}O ($\delta^{18}O_{IVC}$) record for cores EW9302-2JPC and MD95-2010 during the last deglaciation where sufficient independent sea-level constraints exist. To calculate $\delta^{18}O_{IVC}$, we used a eustatic sea-level record (12) to subtract changes in seawater δ^{18}O from the published δ^{18}O record, assuming a relation of 1‰ change in seawater δ^{18}O is equivalent to 130-m sea level (13).

We calculated the change in intermediate water depth δ^{18}O due to the salinity decrease by assuming a meltwater end-member salinity of 0 psu and δ^{18}O of −25‰ to −35‰ (14, 15). We used the freshwater flux from Liu et al. (16) and solved for the ocean flux to match the change in salinity following Carlson (17). Substitution of the δ^{18}O end-member values (−25‰ to −35‰ for meltwater, +1‰ for ocean water) determines the change in δ^{18}O. The modeled approximately 0.5-psu decrease in the Norwegian Sea equates to an approximate 0.4–0.5‰ decrease (−25‰ and −35‰, respectively). The modeled approximately 0.3-psu decrease in the southeast Labrador Sea and in the Caribbean equates to an approximate 0.2–0.3‰ decrease (−25‰ and −35‰, respectively).

5. Possible Contamination of Samples by Dolomite. Because Heinrich layers contain dolomite, negative δ^{18}O excursions in foraminifera associated with Heinrich layers may be due to contamination by fine dolomitic particles (18); similar contamination issues may apply to our Mg/Ca data. Because the flow-through method that we used for Mg/Ca measurements sequentially dissolves foram calcite from the surface inward, it allows us to evaluate any possible sources of contamination, which is its acknowledged strength in making Mg/Ca measurements. In particular, these data (Fig. S2) unequivocally demonstrate that there is no contamination of our forams by detrital dolomite, and thus this is not an issue for our δ^{18}O or Mg/Ca data. For example, Hodell and Curtiss (18) found increases in Ca/Sr associated with detrital carbonate in the Heinrich layers, suggesting that if our samples were contaminated by detrital carbonate, we should see increases in Ca/Sr of our forams. The absence of this signal thus demonstrates that there is no such contamination, indicating that it is not an issue for our δ^{18}O data. Similarly, the absence of a Mg signal in the outer part of our forams unequivocally demonstrates that there is no contamination of any surface coatings by dolomite, although we emphasize that the significance of the flow-through method is to remove any such coating on the shell before collecting data from the inner part of the foram shell, which we used in our study. Finally, we saw no evidence of dissolution of forams or lithic carbonate grains, indicating that there are no dissolution effects.

6. Ocean Model with Ice-Shelf Thermodynamic Coupling. The ocean model is based on the Regional Ocean Modeling System

(ROMS) version 3.0 (19, 20). ROMS is a free-surface, hydrostatic ocean model that solves the 3D primitive equations for a finite-difference lateral grid and a terrain-following vertical coordinate. For a recent application of ROMS with coupling to a thermodynamically active ice shelf, see Dinniman et al. (21).

The model was formulated on the domain shown in Fig. S3. The horizontal grid spacing is $\Delta x \approx 10$ km, and there are 25 vertical levels. Minimum thickness of the water column (ice base to seabed) is set to 200 m. Model bathymetry was based on TOPO12.1 (http://topex.ucsd.edu/marine_topo/mar_topo.html), an updated version of the global gridded bathymetry dataset first reported by Smith and Sandwell (22). The TOPO12.1 grid includes the International Bathymetric Chart of the Arctic Ocean (23).

The ice-shelf geometry follows Hulbe (24): The ice shelf fills Baffin Bay and grounds across Davis Strait, cutting off the northern portion of Baffin Bay, which is then excluded from our model. Ice draft (required for the model) is obtained from 0.85 times the modeled steady-state ice thickness in Hulbe (24).

The bathymetry grid was first smoothed to 10 km to match the final model grid spacing, then smoothed further to reduce errors that arise in the baroclinic pressure gradient calculation in models that use terrain-following vertical coordinate systems (25). See Padman et al. (26) for details on numerical requirements for smoothing and smoothing methodology. The ice-shelf draft fields digitized from Hulbe (24) were already sufficiently smooth.

Model hydrography is derived from a simulation with the National Center for Atmospheric Research Community Climate System Model version 3 (NCAR CCSM3) (16). As initial conditions we use profiles, averaged over 500 y, taken from near the center of the ice-shelf front (Fig. S4), and assume horizontal homogeneity. We ran five states: a "cold" state (model years 19.5–19.0 ka), three intermediate states (18.5–18.0 ka, 18.0–17.5 ka, and 17.5–17.0 ka) and a "warm" state (17.0–16.5 ka). The approximate values of subsurface temperature from CCSM3 for these five periods each averaged over the 400- to 800-m depth range corresponding to ice-shelf draft, are $T_i = -1.1\,^{\circ}\mathrm{C}$, $-1.1\,^{\circ}\mathrm{C}$, $-0.8\,^{\circ}\mathrm{C}$, $+0.6\,^{\circ}\mathrm{C}$, and $+1.7\,^{\circ}\mathrm{C}$, respectively.

The model was forced by barotropic tides (tide height and currents) at the open boundaries. Tides were recalculated for a larger-domain model of the North Atlantic Ocean, using open boundary conditions from the modern global barotropic tide model TPXO7.2 (27). Geometry in the Labrador Sea and Baffin Bay was modified to reflect the presence of the specified ice shelf. We assume that the effect of tides of the change in geometry due to the ice shelf does not extend to the boundaries of the larger-domain model. The addition of tides to the circulation that would develop independently through buoyancy fluxes at the ice-shelf base speeds up model equilibration but, for this case, has little effect on the steady-state basal melt rate distribution.

We use the three-equation formulation of ice/ocean thermodynamic exchange described by Holland and Jenkins (28) as applied in ROMS by Dinniman et al. (21). In our application, the friction velocity is calculated at each time step, and so explicitly includes the effects of time-varying tidal currents as well as the thermohaline circulation, or "plume flow," associated with basal melt.

Vertical mixing elsewhere in the model was parameterized by the Mellor–Yamada level 2.5 turbulence closure scheme (29). Benthic stress was modeled as quadratic drag with $c_d = 0.003$. We used a Laplacian ("harmonic") formulation for the horizontal mixing of momentum and tracers, with coefficients of the lateral viscosity A_H and diffusivity K_H both set to 5 $\mathrm{m^2\,s^{-1}}$.

Maps of predicted basal melt rate M_b (Fig. S4) for the cold (19.5–19 ka) and warm (17–16.5 ka) states show similar structure, with highest rates along southwest Greenland where the inflowing water first meets deeply grounded ice and at the deep grounding line of the Hudson Strait Ice Stream (HSIS). However, the magnitude of M_b for the warm state is about six times higher than for the cold state so that the difference map $\Delta M_b = M_b(\mathrm{warm}) - M_b(\mathrm{cold})$ (Figure S5, *Right*) looks similar to $M_b(\mathrm{warm})$.

Modern ice shelves tend to lose approximately $1/2$ of their mass through basal melting and $1/2$ through calving. The Hulbe model (24) assumed that, at steady state, ice-volume input across the HSIS grounding line (approximately 660 $\mathrm{km^3\,a^{-1}}$) was balanced entirely by calving at a specified ice front (Fig. S3). The shelf-integrated mass loss due to modeled mean basal melt (approximately 0.17 $\mathrm{m\,a^{-1}}$) in the cold state corresponds to approximately 70 $\mathrm{km^3\,a^{-1}}$, or approximately 10% of the total mass loss.

The linear relationship between ice-front CCSM3 temperature T_i and shelf-averaged basal melt rate M_{av} from our five simulations is

$$M_{\mathrm{av}} = 0.54 + 0.34.T_i(\mathrm{ma^{-1}}).$$

From this equation and the time series of T_i at the original temporal resolution of the model output (10 y), we estimate a time history of shelf-integrated mass loss corresponding to the excess melt rate relative to the cold-state value (assumed to represent a steady-state ice shelf). Mass loss begins near 18 ka. Integration of this mass loss in time leads to total removal of the ice shelf near 16.7 ka.

This estimate of collapse time requires several assumptions: (*i*) calving rate remains constant throughout the transition to the warm state, (*ii*) the HSIS ice-volume flux remains constant even as the ice shelf thins, (*iii*) area-averaged basal melt rate follows the above linear relationship to T_i even as the ice-shelf draft decreases by excess melt, (*iv*) the opening of northern Baffin Bay (north of Davis Strait) as the ice shelf thins has no impact on subsequent circulation or melt rate of the modeled portion of the ice shelf, and (*v*) net surface accumulation of mass (snowfall) directly on the ice shelf is an insignificant term in the ice-shelf mass budget under all experienced climate states, or can be incorporated as a revision to the calving flux of approximately 590 $\mathrm{km\,a^{-1}}$. Violation of any of these assumptions will change the integrated mass loss and collapse time in ways that cannot be quantified without fully coupled ocean, glaciological, and atmospheric models.

1. Kristjánsdóttir GB, Lea DW, Jennings AE, Pak DK, Belanger CL (2007) New spatial Mg/Ca-temperature calibrations for three Arctic, benthic foraminifera and reconstruction of north Iceland shelf temperature for the past 4000 years. *Geochem Geophys Geosys* 8:Q03P21 (10.1029/2006GC001425).
2. Quillman U, Marchitto TM, Andrews JT, Jennings AE, Dean WE (2008) *38th International Arctic Workshop, Abstracts and Programs*.
3. Elderfield H, Yu J, Anand P, Kiefer T, Nyland B (2006) Calibrations for benthic foraminiferal Mg/Ca paleothermometry and the carbonate ion hypothesis. *Earth Planet Sci Lett* 250:633–649.
4. Klinkhammer GP, Haley BA, Mix AC, Benway HM, Cheseby M (2004) Evaluation of automatd flow-through time-resolved analysis of foraminifera for Mg/Ca paleothermometry. *Paleoceanography* 19:PA4030 (4010.1029/2004PA001050).
5. Lear CH, Rosenthal Y, Slowey N (2002) Benthic foraminifera Mg/Ca-paleothermometry: A revised core-top calibration. *Geochim Cosmochim Acta* 66:3375–3387.
6. Sosdian S, Rosenthal Y (2009) Deep-sea temperature and ice volume changes across the Pliocene-Pleistocene climate transition. *Science* 325:306–310.
7. Stoner JS, Channell JET, Hillaire-Marcel C, Kissel C (2000) Geomagnetic paleointensity and environmental record from Labrador Sea core MD95-2024: Global marine sediment and ice core chronostratigraphy for the last 110 kyr. *Earth Planet Sci Lett* 183:161–177.
8. Rasmussen TL, Oppo DW, Thomsen E, Lehman SJ (2003) Deep sea records from the southeast Labrador Sea: Ocean circulation changes and ice-rafting events during the last 160,000 years. *Paleoceanography* 18 (10.1029/2001PA000736).
9. Dokken T, Jansen E (1999) Rapid changes in the mechanism of ocean convection during the last glacial period. *Nature* 401:458–461.
10. Hughen KA, et al. (2004) Marine04 marine radiocarbon age calibration, 0–26 cal kyr BP. *Radiocarbon* 46:1059–1086.
11. Benway HM, Mix AC, Haley BA, Klinkhammer GP (2006) Eastern Pacific Warm Pool paleosalinity and climate variability: 0–30 kyr. *Paleoceanography* 21:PA3008, 10.1029/2005PA001208.
12. Bassett SE, Milne GA, Mitrovica JX, Clark PU (2005) Ice sheet and solid earth influences on far-field sea-level histories. *Science* 309:925–928.

13. Schrag DP, et al. (2002) The oxygen isotopic composition of seawater during the Last Glacial Maximum. *Quat Sci Rev* 21:331–342.
14. Remenda VH, Cherry JA, Edwards TWD (1994) Isotopic composition of old ground water from Lake Agassiz: implications for Late Pleistocene climate. *Science* 266:1975–1978.
15. Aharon P (2003) Meltwater flooding events in the Gulf of Mexico revisited: Implications for rapid climate change during the last deglaciation. *Paleoceanography* 18 (10.1029/2002PA0000840).
16. Liu Z, et al. (2009) Transient simulation of last deglaciation with a new mechanism for Bølling-Allerød warming. *Science* 325:310–314.
17. Carlson AE (2009) Geochemical constraints on the Laurentide Ice Sheet contribution to Meltwater Pulse 1A. *Quat Sci Rev* 28:1625–1630.
18. Hodell DA, Curtis JH (2008) Oxygen and carbon isotopes of detrital carbonate in North Atlantic Heinrich Events. *Mar Geol* 256:30–35.
19. Shchepetkin AF, McWilliams JC (2005) The Regional Oceanic Modeling System (ROMS): A split explicit, free-surface, topography-following-coordinate oceanic model. *Ocean Modelling* 9:347–404.
20. Shchepetkin AF, McWilliams JC (2003) A method for computing horizontal pressure-gradient force in an oceanic model with a nonaligned vertical coordinate. *J Geophys Res* 108:3090 (3010.1029/2001JC001047).
21. Dinniman MS, Klinck JM, Smith WW, Jr. (2007) The influence of sea ice cover and icebergs on circulation and water mass formation in a numerical circulation model of the Ross Sea, Antarctica. *J Geophys Res* 112:C11013 (11010.11029/12006JC004036).
22. Smith WHF, Sandwell DT (1997) Global sea floor topography from satellite altimetry and ship depth soundings. *Science* 277:1956–1962.
23. Jakobsson M, et al. (2008) An improved bathymetric portrayal of the Arctic Ocean: Implications for ocean modeling and geological, geophysical and oceanographic analyses. *Geophys Res Lett* 35:L07602, 10.1029/2008GL033520.
24. Hulbe CL (1997) An ice shelf mechanism for Heinrich layer production. *Paleoceanography* 12:711–717.
25. Beckmann A, Haidvogel DB (1993) Numerical simulation of flow around a tall isolated seamount. Part I: Problem formulation and model accuracy. *J Phys Oceanogr* 23:1736–1753.
26. Padman L, Howard SL, Orsi A, Muench RD (2009) Tides of the northwestern Ross Sea and their impact on dense outflows of Antarctic Bottom Water. *Deep Sea Research, Part II* 56:818–834.
27. Egbert GD, Erofeeva SY (2004) Efficient inverse modeling of barotropic ocean tides. *J Oceanic Atmospheric Technol* 19:183–204.
28. Holland DM, Jenkins A (1999) Modelling thermodynamic ice-ocean interactions at the base of an ice shelf. *J Phys Oceanogr* 29:1787–1800.
29. Mellor GL, Yamada T (1982) Development of a turbulence closure model for geophysical fluid problems. *Rev Geophys Space Phys* 20:851–875.

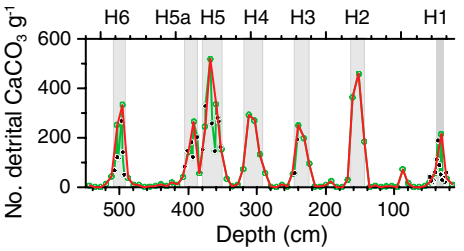

Fig. S1. Detrital carbonate counts from EW9302-2JPC. The original record (1) (red line) is compared to our higher resolution record (green line, with original data shown by green dots and our new data shown by black dots), showing replication of original samples as well as new DC counts.

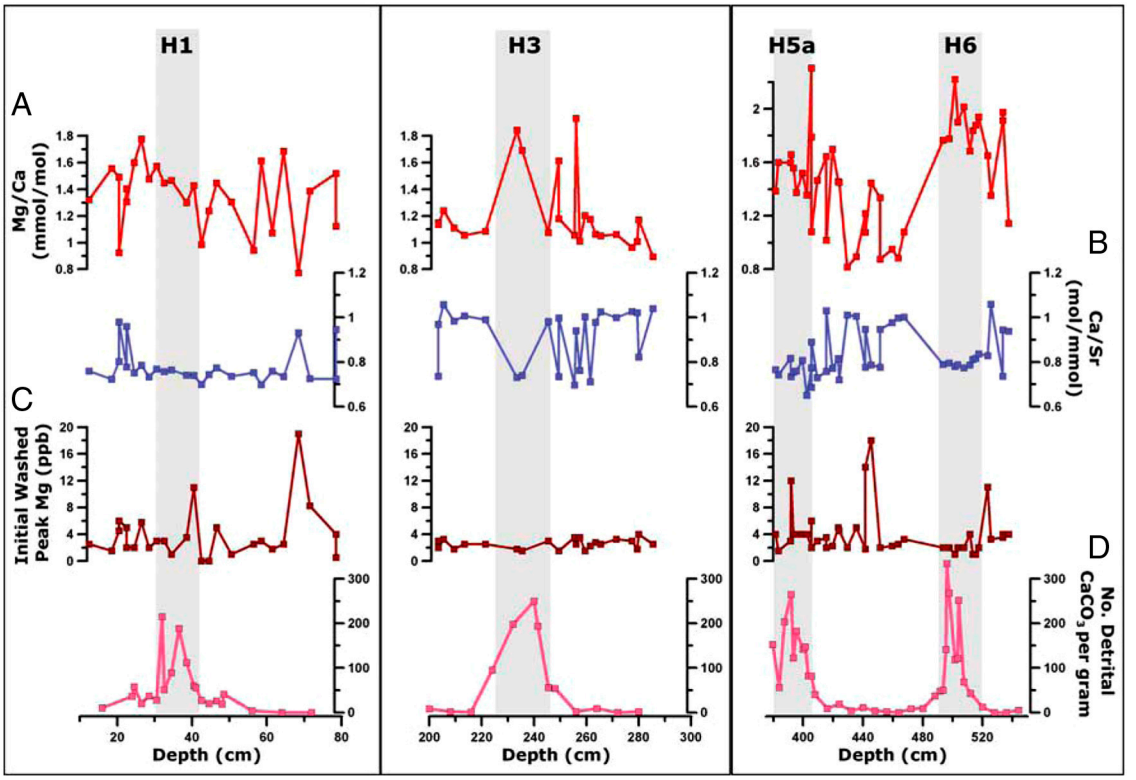

Fig. S2. (*A*) Mg/Ca data, (*B*) Ca/Sr data from the entire foram, (*C*) Mg from the initial outer dissolved part of the foram, and (*D*) carbonate ice rafted debris.

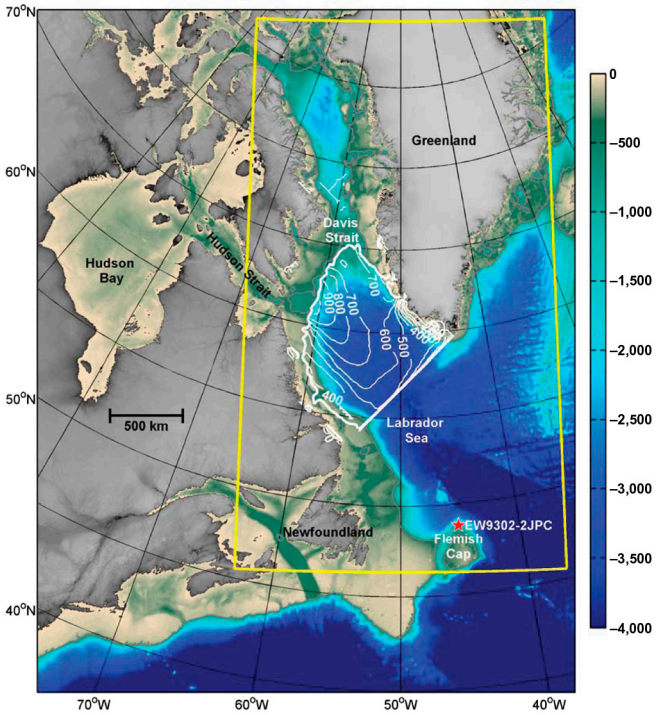

Fig. S3. Modern bathymetry in m (color scale on right) from TOPO12.1. White annotated contours show ice-shelf draft (m). Bold white contour outlines edge of model ice shelf: Baffin Bay north of the ice-shelf grounding line in Davis Strait is treated as land. Yellow outline shows domain of ocean model with coupled ice-shelf thermodynamics.

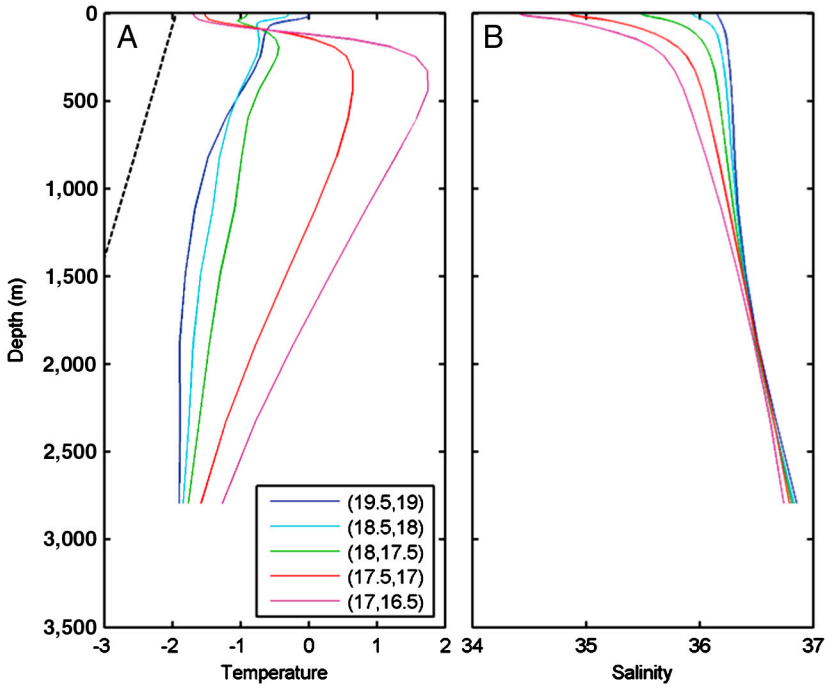

Fig. S4. (*A*) Solid lines show profiles of temperature from NCAR CCSM3 for a model node near the center of the paleo ice front at 56°N, 47.5°W. Temperatures have been averaged over the 500-year time intervals (years BP) listed in the legend. Dashed lines show in situ freezing temperature for a salinity of 35.5. (*B*) As in *A*, for salinity.

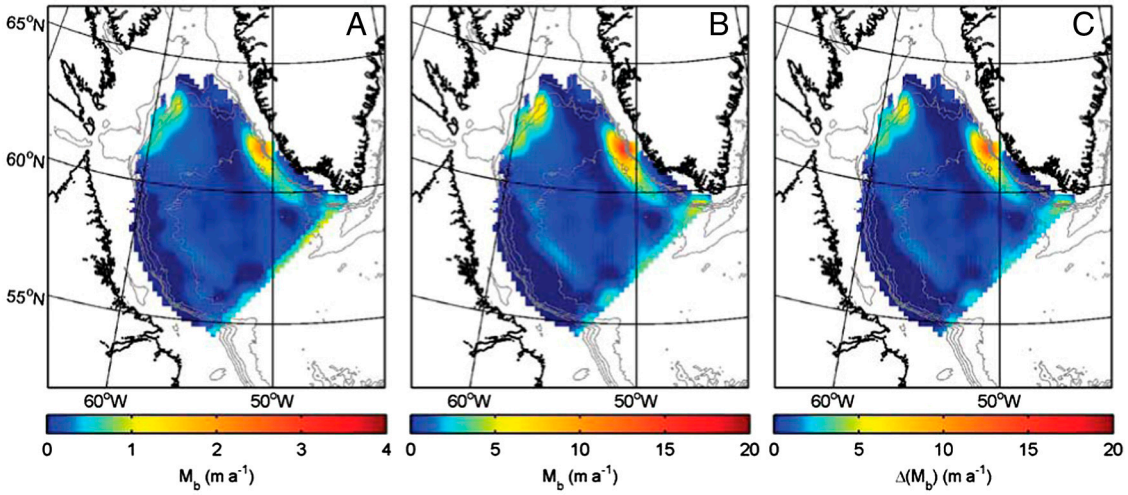

Fig. S5. (*A*) Modeled basal melt rate M_b (m a^{-1}) for cold state 19.5–19 ka. (*B*) Same as *A*, for warm state 17–16.5 ka. (*C*) Difference between warm-state and cold-state basal melt rates, ΔM_b. Note smaller color range for map of cold state M_b.

Table S1. Mg/Ca data for core EW9302-2JPC

Depth, cm				
Midpoint	Age, y	Mg/Ca	BWT, °C	Species
1.5	0	1.798	6.2912	*C. spp.*
1.5	0	1.283	4.8741	*M. barl.*
12.5	11,208	1.321	3.4886	*C. spp.*
18.5	12,954	1.556	4.9771	*C. spp.*
20.5	13,536	1.491	3.0058	*C. lobt.*
20.5	13,536	0.924	2.4782	*M. barl.*
22.5	14,118	1.403	4.0361	*C. spp.*
22.5	14,118	1.306	5.0038	*M. barl.*
24.5	14,700	1.599	5.2249	*C. spp.*
26.5	15,282	1.776	6.1793	*C. spp.*
28.5	15,864	1.476	4.4972	*C. spp.*
30.5	16,446	1.573	5.0759	*C. spp.*
32.5	16,935	1.446	4.3106	*C. spp.*
34.5	17,148	1.467	4.4416	*C. spp.*
38.5	17,573	1.299	3.336	*C. spp.*
40.5	17,786	1.427	4.1903	*C. spp.*
42.5	17,999	0.985	0.8204	*C. spp.*
44.5	18,212	1.238	1.0453	*C. lobt.*
46.5	18,424	1.447	4.3168	*C. spp.*
50.5	18,850	1.303	3.3639	*C. spp.*
56.5	19,488	0.943	0.4243	*C. spp.*
58.5	19,701	1.611	3.9612	*C. lobt.*
61.5	20,020	1.073	−0.2093	*C. lobt.*
64.5	20,309	1.683	4.5194	*C. lobt.*
68.5	20,494	0.772	1.1663	*M. barl.*
71.5	20,632	1.385	2.2093	*C. lobt.*
78.5	20,955	1.518	3.2403	*C. lobt.*
78.5	20,955	1.123	3.9019	*M. barl.*
203.5	29,245	1.149	0.3798	*C. lobt.*
203.5	29,245	1.135	3.9794	*M. barl.*
205.5	29,351	1.241	4.6312	*M. barl.*
209.5	29,563	1.109	3.8103	*M. barl.*
213.5	29,775	1.056	3.4528	*M. barl.*
221.5	30,199	1.086	3.6573	*M. barl.*
233.5	30,835	1.842	6.511	*C. spp.*
235.5	30,941	1.69	5.7281	*C. spp.*
245.5	31,789	1.076	3.5898	*M. barl.*
249.5	32,232	1.613	5.3041	*C. spp.*
249.5	32,232	1.179	4.2571	*M. barl.*
255.5	32,897	1.055	3.4459	*M. barl.*
256	32,952	1.93	7.8545	*M. barl.*
257.5	33,118	1.013	3.1494	*M. barl.*
259.5	33,340	1.203	4.4042	*M. barl.*
261.5	33,561	1.175	4.2323	*M. barl.*
263.5	33,783	1.065	3.5148	*M. barl.*
265.5	34,004	1.05	3.4112	*M. barl.*
271.5	34,669	1.061	3.4873	*M. barl.*
277.5	35,333	0.963	2.7799	*M. barl.*
279.5	35,555	1.009	3.1205	*M. barl.*
280	35,610	1.17	4.2011	*M. barl.*
285.5	36,219	0.894	2.2372	*M. barl.*
325.5	40,649	1.89	6.0976	*C. lobt.*
327.5	40,871	1.194	0.7044	*C. lobt.*
328	40,926	1.36	1.9907	*C. lobt.*
335.5	41,757	1.258	1.2003	*C. lobt.*
351.5	44,694	1.462	2.7811	*C. lobt.*
357.5	45,810	1.951	7.0337	*C. spp.*
359.5	46,182	1.503	3.0988	*C. lobt.*
363.5	46,925	1.339	1.828	*C. lobt.*
377.5	49,529	1.555	3.5017	*C. lobt.*
381.5	50,272	1.387	2.1999	*C. lobt.*
383.5	50,644	1.602	3.8659	*C. lobt.*
391.5	52,132	1.598	3.8349	*C. lobt.*
392	52,225	1.66	4.3154	*C. lobt.*
393.5	52,504	1.557	4.9829	*C. spp.*
395.5	52,876	1.375	3.8529	*C. spp.*
399.5	53,619	1.521	3.2383	*C. lobt.*
402.5	54,177	1.356	3.7264	*C. spp.*

Depth, cm				
Midpoint	Age, y	Mg/Ca	BWT, °C	Species
405.5	54,735	2.307	9.3289	*C. lobt.*
405.5	54,735	1.791	5.3566	*C. lobt.*
405.5	54,735	1.082	3.6304	*M. barl.*
409.5	55,273	1.467	2.8198	*C. lobt.*
415.5	55,566	1.645	4.1991	*C. lobt.*
415.5	55,566	1.0175	3.1817	*M. barl.*
419.5	55,762	1.7	4.6253	*C. lobt.*
423.5	55,957	1.458	2.7501	*C. lobt.*
424	55,982	1.45	2.6881	*C. lobt.*
429.5	56,251	0.816	1.5709	*M. barl.*
435.5	56,544	0.895	2.2454	*M. barl.*
441.5	56,837	1.218	0.8904	*C. lobt.*
441.5	56,837	1.076	3.5898	*M. barl.*
445.5	57,032	1.446	2.6571	*C. lobt.*
451.5	57,326	1.335	1.797	*C. lobt.*
451.5	57,326	0.875	2.0804	*M. barl.*
459.5	57,716	0.951	2.6884	*M. barl.*
463.5	57,912	0.883	2.1469	*M. barl.*
467.5	58,107	1.079	3.6101	*M. barl.*
493.5	59,378	1.766	5.1368	*C. lobt.*
497.5	59,953	1.777	5.222	*C. lobt.*
501.5	61,161	2.223	8.678	*C. lobt.*
503.5	61,766	1.902	6.1906	*C. lobt.*
507.5	62,974	2.016	7.074	*C. lobt.*
511.5	64,182	1.685	4.5091	*C. lobt.*
513.5	64,786	1.838	5.6947	*C. lobt.*
515.5	65,391	1.88	6.0201	*C. lobt.*
517.5	65,995	1.94	6.4851	*C. lobt.*
523.5	67,807	1.65	4.2379	*C. lobt.*
525.5	68,411	1.354	5.2673	*M. barl.*
531.5	70,224	1.012	3.1422	*M. barl.*
533.5	70,828	1.915	6.3178	*C. lobt.*
533.5	70,828	1.976	8.0265	*M. barl.*
535.5	71,432	1.336	5.1696	*M. barl.*
537.5	72,036	1.145	4.0435	*M. barl.*
539.5	72,641	1.514	6.0825	*M. barl.*
541.5	73,245	1.107	3.7971	*M. barl.*
543.5	73,849	1.609	3.9457	*C. lobt.*
543.5	73,849	1.295	4.9421	*M. barl.*
545.5	74,453	1.551	3.4961	*C. lobt.*
545.5	74,453	1.159	4.1322	*M. barl.*
547.5	75,057	1.289	1.4651	*C. lobt.*
547.5	75,057	1.11	3.8169	*M. barl.*
549.5	75,662	2.085	7.6357	*C. lobt.*
549.5	75,662	1.603	6.4995	*M. barl.*

Subsampling for Mg/Ca measurements was done in centimeter intervals.

Table S2. Data for core MD95-2010

Depth, cm					
Midpoint	Age, y	Mg/Ca	Species	BWT, °C	Notes
54.5	12,549	—	—	—	calibrated ^{14}C age
123.5	14,236	1.22	*M. barl.*	4.505	
129.5	14,382	1.549	*M. barl.*	6.249	
133.5	14,479	1.128	*M. barl.*	3.934	
134.5	14,504	1.149	*M. barl.*	4.069	
134.5	14,504	1.62	*C. lobt.*	4.031	
136.5	14,540	—	—	—	calibrated ^{14}C age
146.5	15,242	1.96	*C. spp.*	7.075	
156.5	15,911	2.758	*C. lobt.*	12.853	
159	16,079	2.828	*M. barl.*	10.643	sample interval: 158–160 cm
161.5	16,246	2.95	*C. lobt.*	14.341	
173.5	17,015	—	—	—	calibrated ^{14}C age
192.5	17,841	2.457	*M. barl.*	9.617	
197.5	18,032	—	—	—	calibrated ^{14}C age
199.5	18,063	1.726	*M. barl.*	7.039	
202.5	18,100	1.684	*M. barl.*	6.859	
204.5	18,125	1.54	*M. barl.*	6.207	
206.5	18,150	1.557	*M. barl.*	6.287	
209	18,181	1.535	*M. barl.*	6.183	sample interval: 208–210 cm
213	18,231	1.787	*M. barl.*	7.293	sample interval: 212–214 cm
226.5	18,399	3.673	*C. lobt.*		suspect value; not included
227	18,405	1.922	*M. barl.*	7.824	sample interval: 226–228 cm
233	18,479	1.419	*M. barl.*	5.61	sample interval: 232–234 cm
246	18,641	1.814	*M. barl.*	7.402	sample interval: 245–247 cm
251	18,703	1.725	*M. barl.*	7.035	sample interval: 250–252 cm
300.5	19,312	—	—	—	calibrated ^{14}C age

Subsampling for Mg/Ca measurements was done in centimeter intervals except where indicated.

Table S3. Age-depth data for EW9302-2JPC

Depth, cm	^{14}C Age, y	Error, 1σ	Calibrated ^{14}C Age, y	Error	Notes
16	10,300	100	12,226	257	Vedde Ash
32	13,770	130	16,882	125	
64	17,090	120	20,286	161	
161	20,780	150	24,760	205	
200	24,280	240	29,059	306	
240	26,710	240	31,180	123	
336	36,950	700	41,812	505	
408	—	—	55,200	—	Ash II
496	—	—	59,500	—	H6 Tie Point
544	—	—	74,000	—	Stage 5/4